Journal of
Biomedical Optics

SPIEDigitalLibrary.org/jbo

Live animal myelin histomorphometry of the spinal cord with video-rate multimodal nonlinear microendoscopy

Erik Bélanger
Joël Crépeau
Sophie Laffray
Réal Vallée
Yves De Koninck
Daniel Côté

SPIE

Journal of Biomedical Optics 17(2), 021107 (February 2012)

Live animal myelin histomorphometry of the spinal cord with video-rate multimodal nonlinear microendoscopy

Erik Bélanger,[a,b,c] **Joël Crépeau,**[a,b,c] **Sophie Laffray,**[a] **Réal Vallée,**[a,b,c] **Yves De Koninck,**[a,b,d] **and Daniel Côté**[a,b,c]
[a]Université Laval, Centre de recherche de l'Institut universitaire en santé mentale de Québec, Québec, Canada
[b]Université Laval, Centre d'optique, photonique et laser (COPL), Québec, Canada
[c]Université Laval, Département de physique, de génie physique et d'optique, Québec, Canada
[d]Université Laval, Département de psychiatrie et de neurosciences, Québec, Canada

Abstract. *In vivo* imaging of cellular dynamics can be dramatically enabling to understand the pathophysiology of nervous system diseases. To fully exploit the power of this approach, the main challenges have been to minimize invasiveness and maximize the number of concurrent optical signals that can be combined to probe the interplay between multiple cellular processes. Label-free coherent anti-Stokes Raman scattering (CARS) microscopy, for example, can be used to follow demyelination in neurodegenerative diseases or after trauma, but myelin imaging alone is not sufficient to understand the complex sequence of events that leads to the appearance of lesions in the white matter. A commercially available microendoscope is used here to achieve minimally invasive, video-rate multimodal nonlinear imaging of cellular processes in live mouse spinal cord. The system allows for simultaneous CARS imaging of myelin sheaths and two-photon excitation fluorescence microendoscopy of microglial cells and axons. Morphometric data extraction at high spatial resolution is also described, with a technique for reducing motion-related imaging artifacts. Despite its small diameter, the microendoscope enables high speed multimodal imaging over wide areas of tissue, yet at resolution sufficient to quantify subtle differences in myelin thickness and microglial motility. [DOI: 10.1117/1.JBO.17.2.021107]

Keywords: biomedical optics; endoscopy; fluorescence; microscopy; nonlinear optics; Raman effect.

Paper 11541SS received Sep. 26, 2011; revised manuscript received Nov. 15, 2011; accepted for publication Nov. 28, 2011; published online Mar. 21, 2012.

1 Introduction

The study of neurodegenerative disorders such as multiple sclerosis (MS) is currently hampered by our inability to properly visualize key pathogenic players (blood–brain barrier breakdown, immune cells infiltration, myelin degradation, axonal transection). Although the exact cause is unclear, it is generally accepted that lesions result from infiltrating immune cells that target myelin antigens.[1] Briefly, the purpose of myelin is to ensure efficient saltatory conduction of action potentials over large distances by insulating axons between the nodes of Ranvier, where the action potentials are regenerated. The myelin thickness varies with the axonal diameter and the g-ratio, defined as the axonal diameter divided by the diameter of the axon and its myelin sheath, is around 0.60 to 0.70 across all species.[2] In demyelinating pathologies, the myelin thickness is known to decrease by as much as 20% of its nominal value.[3] Magnetic resonance imaging (MRI) allows the evaluation of the status of myelin sheaths (through T2-weighted MRI and with diffuse tensor imaging) and the blood–brain barrier (with gadolinium enhancement) in the central nervous system, but only at macroscopic levels. Consequently, early signs of diseases and subtle differences between therapies usually go undetected with MRI. Immunohistochemistry applied to *ex vivo* samples can provide sufficient spatial resolution and a variety of contrast agents, but morphological measurements may be affected by deformation artifacts due to fixation, dehydration, paraffin embedding, and mechanical cutting. Additionally, this approach is impractical for studies over large volumes of tissue because of the time required for sample preparation. Moreover, a large number of biological samples at different time points are needed when performing *ex vivo* studies, therefore masking inter-individual variations in the pathology. Hence, *in vivo* cellular imaging techniques are needed to accelerate the study and drug developments for neurodegeneration.

In vivo optical microscopy has demonstrated its importance to study tissue morphology or dynamical processes over the course of days and weeks.[4] Its broad variety of contrast mechanisms, both endogenous and exogenous, makes it particularly appealing for studies involving multiple cell populations. In particular, label-free techniques compatible with multimodal imaging provide a perfect opportunity for studying neurodegenerative disorders. Coherent anti-Stokes Raman scattering (CARS) imaging of myelin is such an endogenous contrast mechanism: it allows for quantitative histomorphometry in live tissue without exogenous contrast agent[5–7] and with a narrow spectral emission, leaving the remaining spectrum for fluorescence imaging. Coupled with miniature objective lenses, it extends the imaging depth and reduces surgery footprint to image neurodegeneration longitudinally over the course of days. Miniature gradient index lenses have been used in studies with various linear and nonlinear imaging modalities such as confocal reflectance and fluorescence, two-photon excitation fluorescence (TPEF), and second harmonic generation.[8–13] For the CARS modality, other strategies have been favored such as fiber optic based delivery,[14–20] miniaturized microscope

---

Address all correspondence to: Daniel Côté, Université Laval, Centre de recherche de l'Institut universitaire en santé mentale de Québec, Québec, Canada. Tel: 418-559-4620; Fax: 418-663-8756; E-mail: daniel.cote@crulrg.ulaval.ca

0091-3286/2012/$25.00 © 2012 SPIE

objectives,[21,22] and scanning fiber approaches,[23] but they are marginally compatible with live animal imaging either because of the low frame rate, the detection geometry, the device size or the single imaging modality limitation meaning that today, CARS microendoscopy is neither common in laboratories nor in clinics.

In this paper, we show that CARS microendoscopy at cellular resolution in live mouse spinal cord can be achieved with a commercially available microendoscope while retaining compatibility with TPEF. We discuss a strategy based on image similarity gating (ISG) to reduce motion-related imaging artifacts. This enables quantification of myelin histomorphometry and microglial motility, both in their native environment, with submicron spatial resolution. The imaging system is shown to be very sensitive to small variations of the *g*-ratio in different axon populations. Using this multimodal microendoscopic approach, static imaging of myelin and axon morphology, in combination with dynamical time-lapse imaging of microglial cells are reported, making it an ideal tool for neurodegenerative disorder studies.

2 Materials and Methods

2.1 *Animal Surgery*

All experimental procedures have been performed in accordance with guidelines from the Canadian Council on Animal Care. C57BL/6 adult mice (25 to 30 g of body weight) either wild type or transgenic, CX3CR1-GFP (Jackson Laboratory, B6.129P-Cx3cr1$^{\mathrm{tm1Litt}}$/J) or Thy1-YFP (Jackson Laboratory, B6.Cg-Tg [Thy1-YFP]16Jrs/J), were anaesthetized with a mixture of ketamine-xylasine (100 mg/kg and 10 mg/kg, respectively, by intraperitoneal injection) supplemented hourly. Body temperature was kept at $37.5 \pm 2\,^{\circ}\mathrm{C}$ with a feedback-controlled heating blanket.

To image the spinal cord *in vivo*, either the lumbar segment L5 was exposed by laminectomy and the meninges gently removed or the intervertebral space between lumbar segments L4 and L5[24] was cleared of muscular tissue and enlarged to a 1.5-mm diameter hole with a surgical drill. The latter intervention gave access to the spinal tissue with the meninges left in place, minimizing surgery invasiveness. A portable stereotaxic frame with two adjustable clamps for vertebral fixation, rostral, and caudal to the exposed section, was mounted on a micromanipulator (Sutter Instrument, MPC-200). An agar pool was formed around the exposed spinal segment and filled with artificial cerebrospinal fluid.

2.2 *Video-Rate Multimodal Nonlinear Microscope*

The laser sources[6] and the custom-made video-rate laser scanning microscope[25] are illustrated in Fig. 1. The laser system consists of an optical parametric oscillator (OPO) (APE, Levante Emerald) pumped by a frequency-doubled Nd:YVO$_4$ mode-locked laser (High Q Laser, picoTRAIN). The pump laser generates a 7-ps, 80-MHz pulse train of 532- and 1064-nm laser light. The OPO is pumped with 5 W of 532-nm laser light.

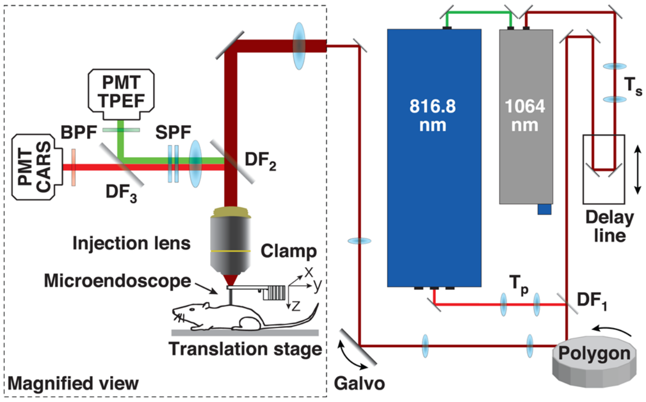

Fig. 1 Laser and imaging system for simultaneous CARS and TPEF imaging with a microendoscope. T_p: pump beam telescope, T_s: Stokes beam telescope, DF$_1$: recombining dichroic filter, DF$_2$ and DF$_3$: detection dichroic filters, SPF: short-pass filter and BPF: band-pass filter.

CARS is a nonlinear process in which two laser beams at two different frequencies drive the emission of an anti-Stokes signal when their frequency difference matches a Raman active vibration of the sample.[26–28] In order to probe the CH$_2$ symmetric stretch vibration of lipids at 2845 cm^{-1}, the OPO is tuned to 816.8 nm and is mixed with a fraction of the 1064-nm laser beam. Both pump and Stokes beams are used as excitation for TPEF, but most of the signal originates from the use of the pump beam. The excitation beams are overlapped in space using a dichroic long-pass filter (Semrock, LP02-1064RU-25) and in time using a delay line before they are sent to the laser scanning microscope. Very critical to the perfect spatial overlap of the two beams at the focal spot, their sizes and divergences are independently adjusted with 2∶1 telescopes to maximize CARS signal generation. Small adjustments of the distance between the lenses making the telescopes compensate for chromatic aberration and/or wavefront mismatch that could arise in the optical path to the focal point. The microscope comprises a raster beam scanner formed by a gold-coated polygonal mirror for the fast axis (Lincoln Laser, DT-36-290-025) and a galvanometer mirror for the slow axis (Cambridge Technology, 6240H). The microscope field of view (FOV) is 187.5 μm by 187.5 μm with a 40× objective lens (Olympus, LUMPlan Fl/IR, 0.8 NA, w).

The system acquires images of 500×500 pixels at a rate of 15 frames per second. The backscattered anti-Stokes signal at 662.8 nm or the fluorescence signal are collected in epi-detection configuration. They are separated from the excitation beams by a dichroic long-pass filter (Semrock, FF735-Di01-25×36) and spectrally filtered from unwanted residual light using two laser block filters (Semrock, FF01-750/SP-25). A dichroic long-pass filter (Semrock, FF605-Di02-25×36) sends the signal to the TPEF detector behind a band-pass filter (Chroma, D545/90m), and the remaining light goes to the CARS detector after being filtered by a band-pass filter (Semrock, FF01-655/40-25). A red-sensitive photomultiplier tube (PMT) (Hamamatsu, R3896) is used for both channels. When transgenic mice are imaged, TPEF and CARS imaging are performed simultaneously.

2.3 *Microendoscope*

The microendoscope is 7.4 mm long, has a diameter of 1.4 mm, a magnification of 4.8× and a working distance of 200 μm (GRINTech, GT-MO-080-018-810, 0.8 NA, w). It is held under the microscope by a clamp (Thorlabs, Micro V-Clamps) attached to a 3 axis stage (Newport, ULTRAlign). A 10× injection lens (Olympus, PLN, 0.25 NA) is used to inject light into the proximal end of the microendoscope with approximately matching numerical aperture (NA, 0.25 *versus* 0.18). The total magnification of the microendoscopic system is 48×, and the FOV is 162.5 μm by 162.5 μm.

2.4 *ISG Procedure*

A post-processing algorithm that alleviates respiration-induced image movement artifacts called ISG has been developed. The method relies on movies of distortion-free frames (e.g., 300 to 450) followed *a posteriori* by a custom-built Matlab routine (Mathworks, R2010a) that computes a two-dimensional (2-D) cross-correlation matrix[29] between a user-selected key frame and every other frames. The maximum of the 2-D cross-correlation matrix is then used as a parameter to select a user-specified amount of similar frames and create a new gated data subset. This subset is then aligned and averaged to a single frame, resulting in an image that is free from motion-related imaging artifacts. All images [except Figs. 2(a) and 2(c)] have been processed using this procedure. The ISG routine is available online at www.dcclab.ca/isg/.

2.5 *Image Processing for Histomorphological Analysis*

Myelin histomorphometry is assessed by computing the g-ratio and the myelin thickness.[30] Image processing to measure these parameters from CARS images is performed with Matlab and ImageJ (NIH, 1.42q), following a previously described method.[7] Briefly, three regions of interest (ROIs), each parallel to a myelinated axon (when present), are selected on all tiles of a 2×2 grid overlaid on every image. The axon and myelinated fiber diameters are determined respectively by the inner and outer edges of the myelin structure. These values are extracted from a cumulative integral of the average line profile. The g-ratio is calculated by dividing the diameter of the axon by that of the fiber. Myelin thickness is half the difference between the axon and the fiber diameters. Because axons are randomly sampled at different positions along their diameter, the g-ratio distribution is skewed toward smaller values.[7]

2.6 *Signal-to-Noise/Background Ratio*

In the case of myelin imaging with the CARS modality, the signal-to-noise ratio (SNR) is defined by the ratio of the mean intensity of a myelin sheath area (signal) to the standard deviation of the corresponding adjacent axonal region (background). Analogously, the signal-to-background ratio (SBR) is obtained by the quotient of the mean intensity of a myelin sheath area to the mean of the corresponding adjacent axonal region.

2.7 *Statistical Analysis*

Values are expressed in terms of mean ± standard error of the mean unless otherwise stated. Statistical analysis of the data was performed using Matlab. Student's t-test and Mann-Whitney U-test were used to evaluate differences between the mean and the median of two distributions respectively.

3 Results

3.1 *Reduction of Motion-Related Imaging Artifacts with ISG*

Figures 2(a) to 2(c) illustrates a typical implementation of the ISG procedure. The original movie has been acquired from the dorsal root at the lumbar enlargement level of a mouse spinal cord and contains 310 frames (Video 1). The user-selected key frame is shown in Fig. 2(a). The graininess of the key frame arises from the low photon count (the shot noise of the PMT), intrinsic to a high-frame-rate acquisition system. Figure 2(b) shows the movement artifact-free image that has been obtained with the ISG procedure while Fig. 2(c) displays the result from averaging every frame composing the movie (without the use of ISG). Comparison among Fig. 2(a), Fig. 2(b), and Fig. 2(c) illustrates the benefits of the ISG procedure in terms of SNR, SBR, and image blurring over unprocessed images. The SNR for the ISG procedure (16.3 ± 2.0) compared to the single frame (4.1 ± 0.2) is significantly higher (five ROIs, one image,

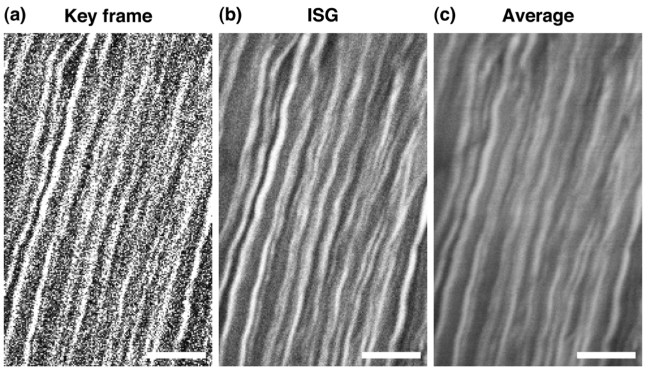

Fig. 2 ISG reduces motion-related artifacts from imaging in living animals. (a) User-selected key frame. (b) Artifact-free image obtained with ISG. (c) Averaging of all frames of the movie. All scale bars are 15 μm. (Video 1, MOV, 9.4 MB). [URL: http://dx.doi.org/10.1117/1.JBO.17.2.021107.1]

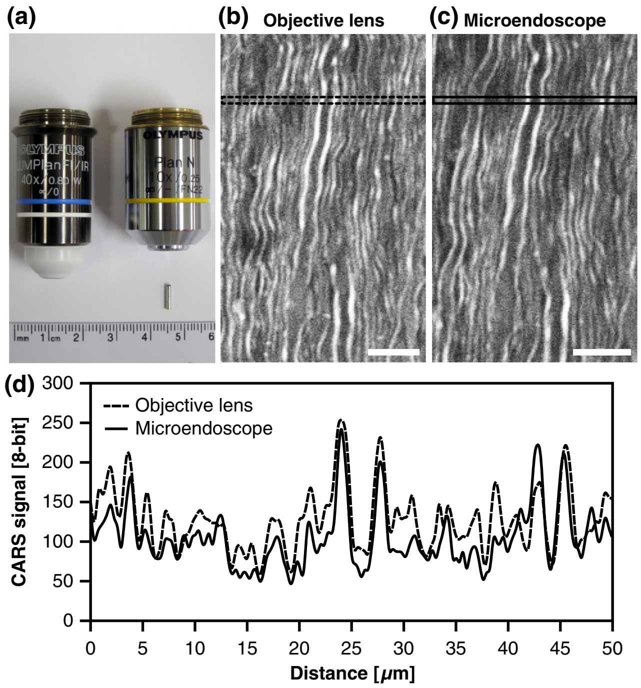

Fig. 3 The use of the microendoscope does not deteriorate *in vivo* CARS image quality. (a) Photo of the 40× objective lens, the 10× injection lens, and the microendoscope. The same spinal cord region was imaged in a live mouse with (b) the objective lens and (c) the microendoscope. (d) Intensity profiles corresponding to the ROIs in (b) and (c). All scale bars are 15 μm.

student's t-test, $p \leq 0.001$). Furthermore, the SBR for the ISG procedure (2.7 ± 0.2) *versus* the averaging (1.7 ± 0.1) is also significantly higher (five ROIs, one image, student's t-test, $p \leq 0.001$). More importantly, myelin sheaths are much sharper when the ISG procedure is used, giving a more reliable morphological representation of the imaged region.

3.2 *Comparison of CARS Images Obtained with the Objective Lens and the Microendoscope*

The objective lens, the injection lens, and the microendoscope are depicted in Fig. 3(a) for size comparison. Figures 3(b) and 3(c) show *in vivo* CARS imaging of myelin sheaths from the dorsal column of a mouse spinal cord at the lumbar enlargement level, acquired with the 40× objective lens and the microendoscope respectively. Laser power at the sample was set to 75 mW (pump) and 25 mW (Stokes) for both conditions. The near infrared wavelengths (816.8 nm and 1064 nm) and the short pixel dwell time ($\simeq 267$ ns) ensure that no damage is done to the tissue. The PMT gain and all other acquisition parameters were kept constant throughout the imaging session. Each image is an average of 30 frames. Signal strength (integrated intensity) is higher in the case of the objective lens by 27% (two images), but optical resolutions (both lateral and axial) are similar due to their identical NA.[12] The SNR ($\simeq 15$) and the SBR ($\simeq 3$) are also comparable for both lenses (10 ROIs, two images, student's t-test, $p \geq 0.05$). The graph in Fig. 3(d) represents the intensity profiles highlighted by the ROIs in Figs. 3(b) (dashed) and 3(c) (full).

3.3 *Video-Rate Multimodal Nonlinear Microendoscopy*

To show the compatibility of the microendoscope with other nonlinear imaging modalities, we imaged the static morphology of axons with TPEF [Fig. 4(a)] simultaneously with myelin sheaths with CARS [Fig. 4(b)] on Thy1-YFP transgenic mice. Figure 4(c) shows the overlay of both modalities. Each image is an average of 30 frames. The graph in Fig. 4(d) represents the intensity profiles of the red and green channels highlighted by the ROI in Fig. 4(c). Their mutually exclusive signal location confirms the intrinsic chemical specificity of the CARS signal for myelin structures.

Next, we performed time-lapse imaging of the basal dynamical behavior of microglial cells with TPEF microendoscopy [Figs. 4(e) red, 4(f), and 4(g)] along with CARS [Fig. 4(e) green] on CX3CR1-GFP transgenic mice. Its highly ramified morphology with no preferential orientation confirms that the cell illustrated in Figs. 4(e) to 4(g) was imaged in an unperturbed environment.[31] Arrowheads highlight regions where the cell extends and retracts its processes as a function of time. The original movie, covering 33 minutes, shows this highly dynamical behavior called surveying state (Video 2). To quantify microglial motility, we measured the length changes and the velocity of

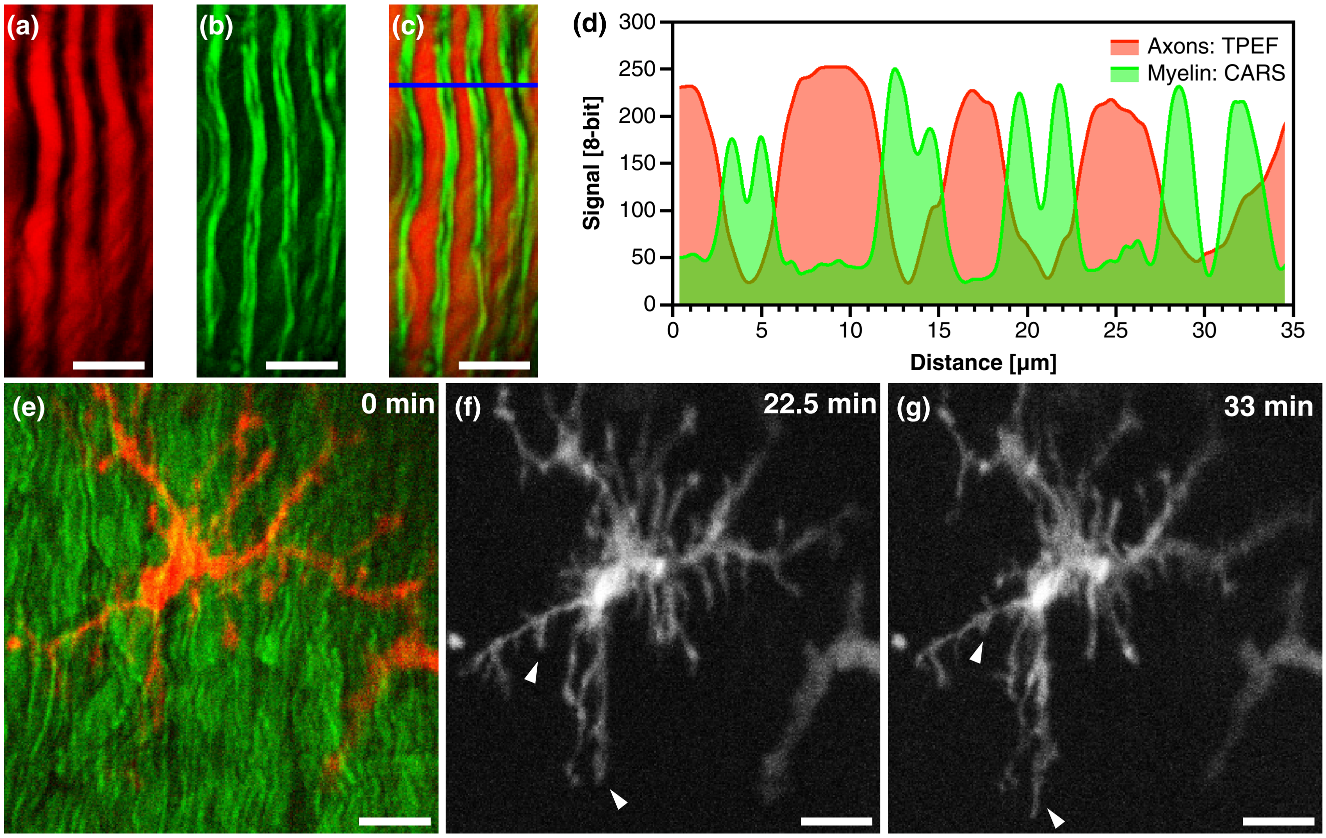

Fig. 4 Video-rate multimodal nonlinear microendoscopy. Static morphology of axons with (a) TPEF of YFP-labeled axons simultaneously with (b) CARS of myelin sheaths. (c) Overlay of both modalities. (d) Intensity profile corresponding to the ROI in (c). Time-lapse imaging of a microglial cell surveying state. (e) TPEF of GFP-labeled microglia (red) and CARS of myelin sheaths (green). (f) and (g) TPEF microendoscopy at subsequent time points. Arrowheads highlight some extensions and retractions of processes. All scale bars are 15 μm. (Video 2, MOV, 0.5 MB). [URL: http://dx.doi.org/10.1117/1.JBO.17.2.021107.2]

individual processes (one cell, nine processes) with MTrackJ. On average, processes extended and retracted 32.27 ± 1.94 μm at a velocity of 1.12 ± 0.09 μm/min, in agreement with literature values.[32,33] Note that microglia remained in their surveillance mode, indicating that imaging through the meninges via the intervertebral space with the microendoscope did not induce noticeable inflammation.

3.4 *Live Animal Myelin Histomorphometry*

In order to validate that the microendoscope is suitable for live animal myelin histomorphometry, a study on five mice was conducted. Images of myelin sheaths in the coronal plane were obtained in the dorsal column and dorsal root. A semi-automated custom-built routine retrieved all relevant morphological parameters,[7] after being processed using the ISG procedure.

Morphological data are shown in Fig. 5. The median of the g-ratio histogram [Fig. 5(a)] was 0.546 ± 0.003 (red, five animals, 56 images, 591 measurements) for axons of the dorsal column while in the dorsal root it was 0.616 ± 0.005 (blue, five animals, 38 images, 357 measurements). It is found that those two axonal populations have a significant difference in the median of the g-ratio distributions (Mann-Whitney U-test, $p \leq 0.001$). The scatter diagram of the g-ratio *versus* the axon caliber [Fig. 5(b)] reveals variations in g-ratio between 0.10 and 0.70 for the dorsal column (circles) and from 0.20 to 0.80 for the dorsal root (squares); their medians were separated by 0.07. Axons from the dorsal column were generally smaller in size (1 to 5 μm diameter) than those from the dorsal root (2 to 10 μm diameter). Finally, Fig. 5(c) shows the myelin thickness histogram for both axonal populations, and it is found that their medians (dorsal column: 0.88 ± 0.01 μm and dorsal root: 1.32 ± 0.02 μm) are significantly different (Mann-Whitney U-test, $p \leq 0.001$). Axons from the dorsal column had a myelin thickness on the order of 0.50 to 1.25 μm while those of the dorsal root ranged from 0.75 to 2.00 μm.

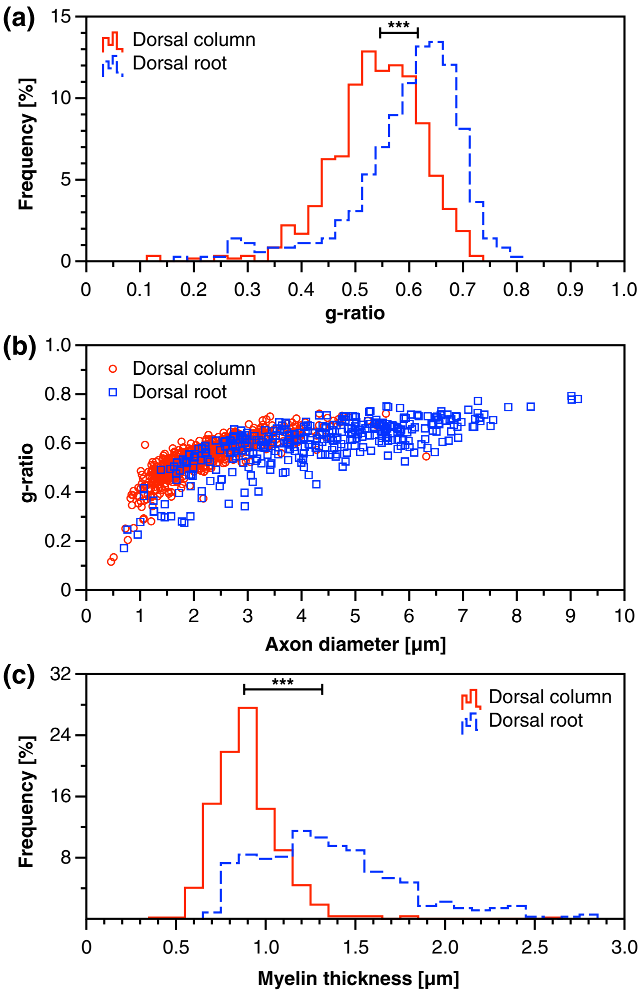

Fig. 5 Live animal myelin histomorphometry differentiates two axonal populations with small differences in g-ratio and myelin thickness. (a) g-ratio histogram. (b) Scatter plot of the g-ratio *versus* the axon diameter. (c) Myelin thickness histogram.

4 Discussion

We have shown that the use of the microendoscope does not affect the SNR and the SBR by comparing CARS images obtained on identical areas of the same sample with a 40× objective lens and the microendoscope [Figs. 3(b) and 3(c)]. The concordance of both intensity profiles [Fig. 3(d)] confirms that the lateral resolution is similar in both configurations, an observation previously made.[12] Thus, the use of the microendoscope does not affect image quality when compared to an objective lens of corresponding NA.

Live animal quantitative microscopy of the spinal cord represents a daunting challenge because of animal motion induced by breathing. Movements of even a few μm during data acquisition can seriously degrade the effective lateral spatial resolution and blur the images. Video-rate acquisition circumvents this issue with distortion-free images, but at the cost of a low photon count, which can only be improved by summing multiple similar frames. To this end, images not similar to a user-determined key frame are automatically removed with the ISG procedure. This results in a significantly higher SBR than the direct average as well as a higher SNR than a single frame. The sharpness of the myelin edges are preserved, enabling precise measurements of histomorphological parameters in live animals. Other elaborated strategies do exist to minimize the importance of movements such as mechanical contention,[34] active control of animal breathing,[35] and adaptive movement compensation.[36] However, for structural imaging where high temporal resolution is not required, ISG is sufficient and much simpler to integrate into existing experimental procedures.

For all the information that CARS histomorphometry provides about myelin,[6,7] it still demands to be placed in context with respect to the many other players of the nervous system (axons, microglia, vasculature, etc.). It is therefore essential for the microendoscope to be fully compatible with other nonlinear imaging modalities, especially TPEF. This capability has been demonstrated here with static imaging of axons morphology and dynamical time-lapse imaging of microglial cells, both obtained with TPEF microendoscopy of transgenic mice.

Finally, from the g-ratio histogram [Fig. 5(a)], it is found that the two axonal populations have a significant difference in the median of the g-ratio distributions: 0.546 ± 0.003 for the dorsal column and 0.616 ± 0.005 for the dorsal root. Also, in Fig. 5(b) the g-ratio tends to increase with axonal diameter. The myelin thickness histograms of Fig. 5(c) showed significantly different medians. Myelin thickness of the dorsal column is on the order of 0.50 to 1.25 μm while that in the dorsal root is 0.75 to 2.00 μm. The shape of the g-ratio distributions, near-normal but skewed toward smaller values, must be interpreted with care: it is known from prior work that indeed, the g-ratio of a myelinated axon decreases for a smaller axonal caliber.[2,30] However, the sampling strategy used in this work (i.e., a collection of random imaging plane) will also bias the g-ratios toward smaller values. In the presence of a single axon population, it is possible to reject smaller g-ratios (i.e., the lower half of the distribution) to obtain a good estimate of the nominal values.[7] However, in the present case, it is expected that the dorsal column and dorsal root populations are not composed of single axonal caliber. Hence because the effect due to random imaging plane sampling cannot be unambiguously separated from the effect that arises from having a population with multiple axonal calibers, the complete g-ratio distributions are used for comparison. It is shown in this case that indeed, the medians of each distribution are significantly different. Since it is known that myelin thickness can decrease by as much as 20% in MS, the technique as presented can provide sufficient precision to differentiate two populations of axons with subtle differences in g-ratio or myelin thickness.

5 Conclusion

We have demonstrated live animal myelin histomorphometry with video-rate CARS microendoscopy with a device compatible with multimodal imaging. The use of this microendoscope maintains image quality and lateral resolution when compared to an objective lens of similar NA. Image movement artifacts caused by breathing in living animals are eliminated using a numerical ISG approach that could be implemented thanks to video-rate acquisition. The microendoscope is shown to possess a spatial resolution sensitive to small variations in g-ratio and myelin thickness between different axon populations, and sufficient to detect initial demyelination and subsequent remyelination in neurodegenerative disorders such as MS. The multimodality is demonstrated with TPEF static imaging of axons morphology and dynamic time-lapse imaging of microglial cells, enabling minimally invasive time-lapse imaging of neurodegenerative disorders with CARS as a myelin imaging modality.

Acknowledgments

This work was supported by a grant from the Collaborative Health Research Projects (CHRP) Program co-funded by the Natural Science and Engineering Research Council (NSERC) and the Canadian Institutes of Health Research (CIHR), a CIHR regenerative medicine emerging team grant, the Canadian Foundation for Innovation (CFI), the Canadian Institute for Photonics Innovation (CIPI), and the Krembil Foundation. D. Côté is the holder of a Canada Research Chair in biophotonics. Y. De Koninck is a Chercheur national of the Fonds de la recherche en santé du Québec (FRSQ). This investigation was supported by a Dr. William J. McIlroy studentship from the Multiple Sclerosis Society of Canada (MSSOC) awarded to E. Bélanger and the Fonds québécois de recherche sur la nature et les technologies (FQRNT) doctoral scholarship held by J. Crépeau. S. Laffray was supported by a fellowship from the CIHR Neurophysics training program. We would like to thank S. Bégin and O. D. Therrien for their critical reading of the manuscript.

References

1. J. H. Noseworthy et al., "Multiple sclerosis," *N. Engl. J. Med.* **343**(13), 938–952 (2000).
2. D. L. Sherman and P. J. Brophy, "Mechanisms of axon ensheathment and myelin growth," *Nat. Rev. Neurosci.* **6**(9), 683–690 (2005).
3. J. Guy et al., "Maintenance of myelinated fibre g ratio in acute experimental allergic encephalomyelitis," *Brain* **114**(Pt. 1A), 281–294 (1991).
4. T. Misgeld and M. Kerschensteiner, "*In vivo* imaging of the diseased nervous system," *Nat. Rev. Neurosci.* **7**(6), 449–463 (2006).
5. H. Wang et al., "Coherent anti-Stokes Raman scattering imaging of axonal myelin in live spinal tissues," *Biophys. J.* **89**(1), 581–591 (2005).
6. E. Bélanger et al., "Quantitative myelin imaging with coherent anti-Stokes Raman scattering microscopy: alleviating the excitation polarization dependence with circularly polarized laser beams," *Opt. Express* **17**(21), 18419–18432 (2009).
7. E. Bélanger et al., "*In vivo* evaluation of demyelination and remyelination in a nerve crush injury model," *Biomed. Opt. Express* **2**(9), 2698–2708 (2011).
8. P. Kim et al., "*In vivo* confocal and multiphoton microendoscopy," *J. Biomed. Opt.* **13**(1), 010501 (2008).
9. J. C. Jung et al., "*In vivo* mammalian brain imaging using one- and two-photon fluorescence microendoscopy," *J. Neurophysiol.* **92**(5), 3121–3133 (2004).
10. J. C. Jung and M. J. Schnitzer, "Multiphoton endoscopy," *Opt. Lett.* **28**(11), 902–904 (2003).
11. M. E. Llewellyn et al., "Minimally invasive high-speed imaging of sarcomere contractile dynamics in mice and humans," *Nature* **454**(7205), 784–788 (2008).
12. R. P. J. Barretto, B. Messerschmidt, and M. J. Schnitzer, "*In vivo* fluorescence imaging with high-resolution microlenses," *Nat. Methods* **6**(7), 511–512 (2009).
13. R. P. J. Barretto et al., "Time-lapse imaging of disease progression in deep brain areas using fluorescence microendoscopy," *Nat. Med.* **17**(2), 223–228 (2011).
14. H. Wang, T. B. Huff, and J.-X. Cheng, "Coherent anti-Stokes Raman scattering imaging with a laser source delivered by a photonic crystal fiber," *Opt. Lett.* **31**(10), 1417–1419 (2006).
15. F. Légaré et al., "Towards CARS endoscopy," *Opt. Express.* **14**(10), 4427–4432 (2006).
16. M. Balu et al., "Fiber delivered probe for efficient CARS imaging of tissues," *Opt. Express* **18**(3), 2380–2388 (2010).
17. Z. Wang et al., "Delivery of picosecond lasers in multimode fibers for coherent anti-Stokes Raman scattering imaging," *Opt. Express* **18**(12), 13017–13028 (2010).
18. Z. Wang et al., "Coherent anti-Stokes Raman scattering microscopy imaging with suppression of four-wave mixing in optical fibers," *Opt. Express* **19**(9), 7960–7970 (2011).
19. S. Brustlein et al., "Double-clad hollow core photonic crystal fiber for coherent Raman endoscope," *Opt. Express* **19**(13), 12562–12568 (2011).
20. Z. Wang et al., "Use of multimode optical fibers for fiber-based coherent anti-Stokes Raman scattering microendoscopy imaging," *Opt. Lett.* **36**(15), 2967–2969 (2011).
21. H. Wang et al., "Increasing the imaging depth of coherent anti-Stokes Raman scattering microscopy with a miniature microscope objective," *Opt. Lett.* **32**(15), 2212–2214 (2007).
22. S. Murugkar et al., "Miniaturized multimodal CARS microscope based on MEMS scanning and a single laser source," *Opt. Express* **18**(23), 23796–23804 (2010).
23. B. G. Saar et al., "Coherent Raman scanning fiber endoscopy," *Opt. Lett.* **36**(13), 2396–2398 (2011).
24. S. L. Hostikka, J. Gong, and E. M. Carpenter, "Axial and appendicular skeletal transformations, ligament alterations, and motor neuron loss in Hoxc10 mutants," *Int. J. Biol. Sci.* **5**(5), 397–410 (2009).
25. I. Veilleux et al., "*In vivo* cell tracking with video rate multimodality laser scanning microscopy," *IEEE J. Sel. Top. Quantum Electron.* **14**(1), 10–18 (2008).
26. C. Evans and X. S. Xie, "Coherent anti-Stokes Raman scattering microscopy: chemical imaging for biology and medicine," *Annu. Rev. Anal. Chem.* **1**, 883–909 (2008).

27. S. Bégin et al., "*In vivo* optical monitoring of tissue pathologies and diseases with vibrational contrast," *J. Biophotonics* **2**(11), 632–642 (2009).
28. J. P. Pezacki et al., "Chemical contrast for imaging living systems: molecular vibrations drive CARS microscopy," *Nat. Chem. Biol.* **7**(3), 137–145 (2011).
29. M. Guizar-Sicairos, S. T. Thurman, and J. R. Fienup, "Efficient subpixel image registration algorithms," *Opt. Lett.* **33**(2), 156–158 (2008).
30. R. L. Friede and W. Beuche, "A new approach toward analyzing peripheral nerve fiber populations. I. Variance in sheath thickness corresponds to different geometric proportions of the internodes," *J. Neuropathol. Exp. Neurol.* **44**(1), 60–72 (1985).
31. U.-K. Hanisch and H. Kettenmann, "Microglia: active sensor and versatile effector cells in the normal and pathologic brain," *Nat. Neurosci.* **10**(11), 1387–1394 (2007).
32. D. Davalos et al., "ATP mediates rapid microglial response to local brain injury *in vivo*," *Nat. Neurosci.* **8**(6), 752–758 (2005).
33. A. Nimmerjahn, F. Kirchhoff, and F. Helmchen, "Resting microglial cells are highly dynamic surveillants of brain parenchyma *in vivo*," *Science* **308**(5726), 1314–1318 (2005).
34. D. Davalos et al., "Stable *in vivo* imaging of densely populated glia, axons and blood vessels in the mouse spinal cord using two-photon microscopy," *J. Neurosci. Methods* **169**(1), 1–7 (2008).
35. M. Kerschensteiner et al., "*In vivo* imaging of axonal degeneration and regeneration in the injured spinal cord," *Nat. Med.* **11**(5), 572–577 (2005).
36. S. Laffray et al., "Adaptive movement compensation for *in vivo* imaging of fast cellular dynamics within a moving tissue," *PLoS One* **6**(5), e19928 (2011).